ISSN 0021-3640, JETP Letters, 2021, Vol. 113, No. 2, pp. 75–81. © Pleiades Publishing, Inc., 2021.
Russian Text © The Author(s), 2021, published in Pis'ma v Zhurnal Eksperimental'noi i Teoreticheskoi Fiziki, 2021, Vol. 113, No. 2, pp. 84–91.

OPTICS
AND LASER PHYSICS

Diffraction on a Microbubble and the Morphology of the Silicon Surface Irradiated through Glycerol by a Pair of Femtosecond Laser Pulses

N. A. Inogamov[a, b, c, *], **S. A. Romashevskiy**[b], **A. I. Ignatov**[a, d], **V. V. Zhakhovsky**[a, b], **V. A. Khokhlov**[c], **E. M. Eganova**[e], **E. A. Pershina**[e], **and S. I. Ashitkov**[b]

[a] *All-Russia Research Institute of Automatics, Moscow, 127055 Russia*
[b] *Joint Institute for High Temperatures, Russian Academy of Sciences, Moscow, 125412 Russia*
[c] *Landau Institute for Theoretical Physics, Russian Academy of Sciences, Chernogolovka, Moscow region, 142432 Russia*
[d] *National Research Moscow State University of Civil Engineering, Moscow, 129337 Russia*
[e] *Institute of Nanotechnologies of Microelectronics, Russian Academy of Sciences, Moscow, 119991 Russia*
**e-mail: nailinogamov@gmail.com*

Received November 26, 2020; revised December 3, 2020; accepted December 3, 2020

The effect of two successive laser pulses on silicon placed in glycerol has been studied experimentally and numerically with electromagnetic, hydrodynamic, and atomistic simulation programs. It has been shown that a microbubble in the liquid is formed on the surface after the first pulse; then, the second pulse whose width is comparable with the diameter of the microbubble is diffracted on this microbubble. The calculated diffraction pattern and light intensity distribution on the silicon surface indicate that the maximum intensity at the diffraction peaks can be noticeably higher than the intensity on the axis of the incident Gaussian beam. An increase in the intensity concentrated in one bright narrow ring around the microbubble results in the formation of a characteristic groove surrounded by ridges on silicon. The molecular dynamics simulation has shown that intense heating at the diffraction peak is responsible for the melting and displacement of the melt from the center of heating. This leads to the formation of grooves with ridges having a profile similar to that measured in the experiment.

DOI: 10.1134/S0021364021020065

1. INTRODUCTION

Fundamental problems of the physics of interaction of radiation with matter are directly connected with modern technologies of electronics, optoelectronics, photonics, plasmonics, etc. (photons as a tool of processing and creation at a nanometer level). The solution of a fundamental problem further certainly increases the level of technological development. Our work (optical nanolithography in a liquid) concerns, on one hand, laser ablation in a liquid [1–4] and, on the other hand, the nanostructuring of the surface under tightly focused radiation [5–11]. The results of the work are presented in Figs. 1 and 2. The method allows processing the surface at scales much smaller than the wavelength in vacuum. Details of the calculations whose results are shown in Figs. 1 and 2 are described in Sections 3–5.

In this work, we consider features of the interaction of two femtosecond laser pulses with the surface of a material (silicon) immersed in a viscous liquid (glycerol). In contrast to irradiation in a gas medium or vacuum, the action of one pulse heats not only the surface layer of the material in the liquid but also a thin adjacent layer of the liquid, which finally leads to the formation of a bubble. This phenomenon is well known in studies of laser ablation in the liquid, which is actively used to obtain chemically pure nanoparticles [1–4]. On one hand, the hot layer of the liquid (diffusely mixed with the material of the target) is a specific "reactor," where nanoparticles are formed [12, 13]; the bubble is formed from the hot layer. On the other hand, this bubble is a negative factor (for the production of nanoparticles) because it screens the surface of the material from the action of subsequent pulses.

On the contrary, we analyze here the spatial modulation of the intensity distribution for the second femtosecond laser pulse on an obstacle in the form of a microbubble (see Figs. 1 and 2). Thus, the bubble in this case is a positive factor. The bubble is formed in the liquid near the surface of the material irradiated by the first pulse [14, 15]. Modulation results in the formation of circular structures on the surface of the material. They are projections (stamps in the target) of the ring diffraction pattern caused by the scattering of

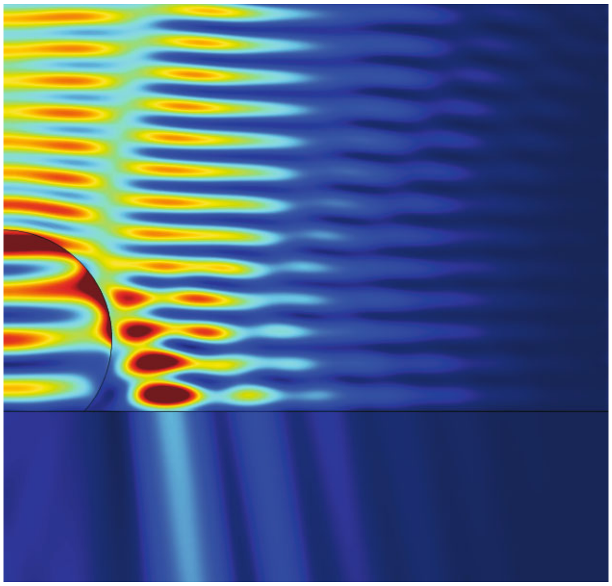

Fig. 1. (Color online) Distribution of the electric field intensity $I(x, z)$ (in arbitrary units) at the diffraction of a linearly polarized Gaussian beam on the bubble with a radius of 1.2 μm in glycerol. The bubble in the form of a spherical segment lies on the planar surface of silicon so that the distance from the center of the sphere to the surface is 0.8 μm. The Gaussian beam is incident from above (from glycerol) and its radius at the $1/e$ intensity level is 3 μm. The wavelength of light in glycerol is 704 nm. The distribution $I(x, z)$ is given in the plane that passes through the center of the sphere, is normal to the surface of silicon, and is parallel to the polarization of the beam.

the second femtosecond laser pulse on the bubble. Only the brightest ring strongly changes the profile of the surface (see Fig. 2).

It is important that radiation passes through the liquid (otherwise, the microbubble would not be formed). Thus, our problem refers to ablation in the liquid with the inevitable formation of the bubble. However, the parameters of the problem formulated in Figs. 1 and 2 are strongly different from the usual parameters of ablation in the liquid [1–4]. The differences are as follows: (i) tight focusing: the radius of the focal spot by the Gaussian beam is 3 μm, whereas it is usually from 100 μm to 1 mm, and (ii) the ultrasmall and long-lived bubble: the radius of the bubble under the weakest external action is an order of magnitude smaller than the radius of the focal spot.

The existence of the bubble and diffraction on it were supposed for the first time in experimental work [14]; see also Section 2. This hypothesis is theoretically proved in this work. In Section 3, we reveal why the bubble appears and why it is so small. The diffraction of the incident electromagnetic wave of the Gaussian beam on the microbubble is analyzed in Section 4. Section 5 describes the simulation of the manifestation of the bright diffraction ring on the surface of the target.

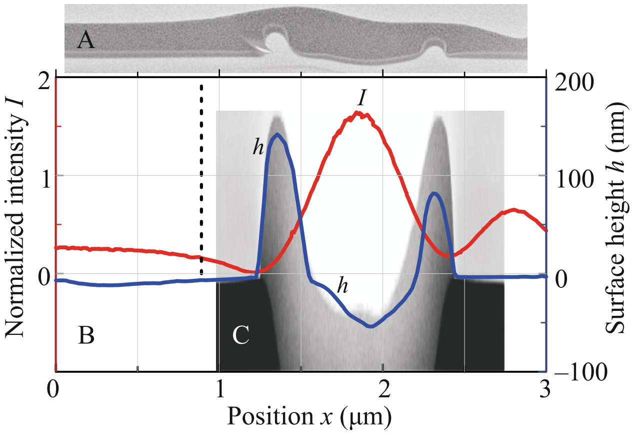

Fig. 2. (Color online) (A) Transmission electron microscopy image (see Section 2) of the cross section of the circular groove surrounded by asymmetric inner and outer ridges. The structure is formed after the action of the second femtosecond laser pulse diffracted on the microbubble. (B) (Red line) Distribution of the normalized intensity $I(x, z = -20 \text{ nm})$ at a depth of 20 nm under the surface of silicon. The distribution $I(x, z)$ in glycerol and silicon is shown in Fig. 1. The maximum of the red line corresponds to the bright diffraction fringe in silicon in Fig. 1. The intensity I is given in units of the value $I_G(x = 0, z = -20 \text{ nm})$ corresponding to the Gaussian beam I_G in the case without the bubble. The profile of the surface shown in Fig. 2A is presented by the blue line (measured by an atomic force microscope). The maximum depth of the circular groove is 50 nm and the height of the ridges is 80–140 nm. (C) Molecular dynamics density distribution in gray tones in the plane intersecting the groove transversely (the curvature of the groove is disregarded); consequently, ridges are symmetric in the molecular dynamics simulation (Section 5). The dashed vertical straight line indicates the rightmost point of the contact of the bubble (truncated sphere) with silicon (see Fig. 1).

2. EXPERIMENT

The source of radiation was an ytterbium fiber laser generating linearly polarized pulses with the duration $\tau_L = 270$ fs at a wavelength of 1028 nm with the repetition frequency up to 5 kHz. The radiation intensity distribution in the cross section of the beam is Gaussian. The laser beam was focused by a micro-objective (×20/0.5) into a spot 6 μm in diameter at the $1/e$ level on the surface of the sample along the normal to it. The target was a polished n-type silicon plate with the [111] crystallographic orientation and roughness $Ra = 0.1$ nm (arithmetic average deviation of the profile). The sample was placed in a Petri dish filled with glycerol. The thickness of the glycerol through which laser radiation passes is 0.9 mm. The experimental scheme was reported in [14].

The surface of silicon immersed in glycerol was irradiated by two identical pulses separated by a time delay of 200 μs. The energy in both pulses was varied by means of a half-wave plate and a polarizer. The energy density (fluence F) on the surface of the sample in the Gaussian spot was varied from $F_0 = 0.6F_\mathrm{a}$ to $1.7F_\mathrm{a}$, where F_0 is the incident energy density in the center of the spot and $F_\mathrm{a} = 0.44$ J/cm^2 is the ablation threshold of silicon for a single action in glycerol at the wavelength $\lambda = 1028$ nm in vacuum, which is determined using the method from [16].

To study the topography of the modified surface, we used an atomic force microscope with the radius of the scanning probe <10 nm in the semicontact mode. The vertical resolution is 0.05 nm. An example of application of the atomic force microscope is shown by the blue line in Fig. 2B. To analyze the near-surface layers and subsurface structure changes, we used transmission electron microscopy (see Fig. 2A). To this end, a 100-nm-thick lamel was cut by a focused ion beam.

Figure 2 shows the structure obtained after the action of two femtosecond laser pulses with $F_0 = 1.02F_\mathrm{a}$. After the action of the first femtosecond laser pulse on the surface, a parabolic microdimple with a diameter of 4 μm is formed [15]. The depth of the microdimple (6 nm) and the height of the ridge around it (7 nm) are much smaller than its diameter. For this reason, the existence of this small relief was neglected in the electrodynamic calculation. As mentioned above, the first femtosecond laser pulse forms the bubble. Because of the action of the second femtosecond laser pulse on the same region, a much deeper (compared to the relief after the first femtosecond laser pulse) circular dimple surrounded by high ridges is formed on the surface as a result of the diffraction on the bubble (Fig. 2). The sharp deepening of the relief at a quite small increase in the fluence compared to F_0 (by a factor of 1.6, the red line in Fig. 2B) is due primarily to a change in the geometry and a decrease in the size: a diffraction ring with a width of 0.6 μm (the FWHM of the peak in the red line) is formed instead of the focal spot 6 μm in diameter.

3. SIZES OF THE MICROBUBBLE

The bubble is not yet formed during irradiation by the first femtosecond laser pulse (it is formed later, after the end of the first pulse), and the problem of the interaction of the first femtosecond laser pulse with matter is standard. The depth D of radiation absorption in silicon at room temperature is large (microns). The rate of ionization of valence electrons through the gap to the conduction band and, correspondingly, the rate of increase dn/dt of the electron–hole plasma density n increases with the intensity of the laser pulse. The depth $D(t)$ decreases with time. The refractive index varies with the plasma density $n(z,t)$, which depends on the time and the depth z measured from the interface with glycerol $z = 0$. The density is maximal at the interface $z = 0$. The density $n(z = 0,t)$ increases during the action of the pulse.

At the intensities used in this work, the density $n(z = 0,t)$ exceeds the critical density at the time t_h during the action of the pulse: $t_h < \tau_\mathrm{L}$. The critical density n_cr is the density at which the plasma frequency $\sqrt{4\pi n_\mathrm{cr}(z = 0,t)e^2/m}$ exceeds the frequency of laser radiation. In this case, the thickness D decreases from several thousand nanometers to several tens of nanometers, and the situation becomes similar to the situation in metals with the absorption of radiation in the skin layer.

We performed series of hydrodynamic and molecular dynamics simulations where the stage of an increase in the density n to the critical value n_cr was omitted. This stage is insignificant for the description of heating and subsequent hydrodynamic motion because the heating of the thin (tens of nanometers) surface layer occurs in the time $t > t_h$ during the action of femtosecond laser pulses. Meanwhile, the hydrodynamic motion begins much later after the end of femtosecond laser pulses: $t \sim t_s \gg \tau_\mathrm{L}$, $t_s \sim 10$ ps and $\tau_\mathrm{L} = 0.27$ ps. Our hydrodynamic and molecular dynamics simulations describe the situation after the metallization of the surface layer of silicon at $t > t_h$, $n > n_\mathrm{cr}$. For the simulation, we used the aluminum–water pair that we previously studied for other applications. The ratio of acoustic impedances for this pair is $Z_\mathrm{Al}/Z_{\mathrm{H_2O}} = 9.5$, which is close to the ratio for the silicon-glycerol pair $Z_\mathrm{Si}/Z_\mathrm{Gl} = 6.3$. The characteristics of motion will be similar for these two pairs.

The main question is: How can we obtain such a small bubble with a radius of several hundred nanometers? We detected a new nontrivial effect: the liquid is mechanically separated from the target at absorbed fluences F_abs below the ablation threshold F_a. This occurs because the boundary of the target stops and returns back owing to cohesion in the condensed material of the target at $F_\mathrm{abs} < F_\mathrm{nucl}$ (or owing to the combined action of cohesion and surface tension at $F_\mathrm{nucl} < F_\mathrm{abs} < F_\mathrm{a}$, where F_nucl is the nucleation threshold above which vital nuclei of the vapor phase appear in the melt), whereas the liquid continues to move by inertia. The indicated breakdown of the junction occurs in times about several acoustic time scales in the target $t_\mathrm{s} = d_T/c_\mathrm{s}$, where d_T is the thickness of the heated layer (20–40 nm) and c_s is the speed of sound in the target. Here, $t_\mathrm{s} \sim 10$ ps; i.e., the separation (breakdown of the liquid–target junction) occurs at an early stage. As a result, the thermal flux from the hot target to the liquid decreases sharply. The thickness of the heated layer of the liquid z_T decreases correspondingly. Consequently, the radius R of the bubble, which is later formed from the liquid of this layer, decreases.

Such worsening of heat transfer is impossible under usual conditions of femtosecond ablation in the liquid [13] because irradiation is performed much above the

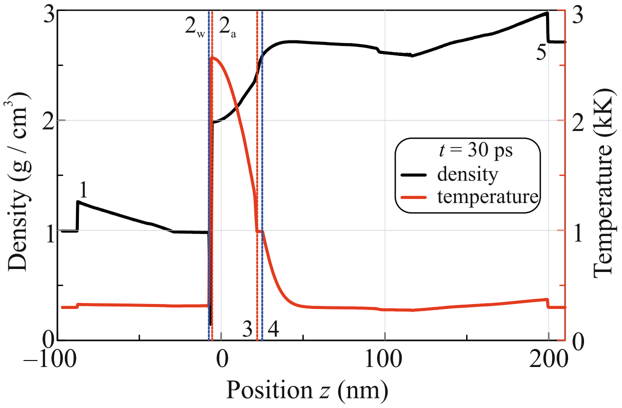

Fig. 3. (Color online) (Black line) Density and (red line) temperature profiles after the separation of the liquid from the target obtained in the hydrodynamic calculation: (1) the shock wave in water; (2) the H_2O–Al interface with the initial position $z = 0$; (3–4) the Al melting region with the liquid and solid phases to the left and right of it, respectively; and (5) the shock wave in the target. The interface is split with the formation of two shores 2_w and 2_a on the sides of water and aluminum, respectively. A uniform flow layer in water appears, which is adjacent to the interface 2_w and is expanded behind the shock wave in water at the speed of sound.

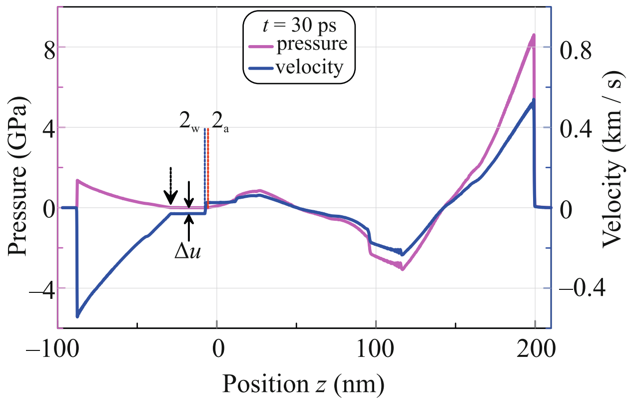

Fig. 4. (Color online) (Red line) Density and (blue line) velocity profiles after the formation of the 2_w–2_a gap between H_2O and Al in the hydrodynamic calculation. The pressure in the empty gap (evaporation is small) and in water and aluminum regions adjacent to the gap is zero. The zero pressure segment in water is located between the left arrow and point 2_w. The double arrow indicates the velocity Δu of the leftward displacement of the water boundary 2_w; see the main text.

ablation threshold F_a. At $F_{abs} > F_a$, thermal contact is not lost and heating continues for a long time; therefore, the radius of the bubble R is larger. In the case of nanosecond ablation in the liquid, pressures are always positive (regions of negative or zero pressures are absent, Lagrange particles in a chain are always attached to each other), and mechanical breakdowns (separation) are absent. The separation of H_2O from Al is illustrated in Figs. 3 and 4. The edge of water moves to the left at the velocity Δu = 30 m/s. The formation time $R/\Delta u$ of the bubble with the radius $R \sim 1$ μm is roughly estimated as 30 ns.

The calculations whose results are shown in Figs. 3 and 4 were performed using the hydrocode from [13]. Details are beyond the scope of this work and require additional presentation. The parameters of the problem are described in Section 2. Aluminum is described using a broadband equation of state [17–21]. Water is simulated using a Mie–Grüneisen-type equation (see [13, 22]), which approximates well the mechanical properties of water.

In our case, the hydrocode ignores the thermal conductivity of water (although the temperature of the target surface is high, see Fig. 3). Consequently, the heating of water is due only to dissipation in a shock wave. This heating is small at our amplitude of the shock wave. Correspondingly, the 2_w–2_a gap in Figs. 3 and 4 is not filled with water vapor and separation results in the vanishing of the pressure.

Another series of simulations was performed using the molecular dynamics code (see Section 5). Here, the atomic thermal conductivity of the liquid is taken into account. We note that the parameters of water and glycerol are close: the speeds of sound differ by one-third, the densities differ by one-fourth, the surface tensions are approximately the same, and the critical parameters of glycerol/water are T_c = 850/647 K and p_c = 75/220 atm. The viscosities are strongly different, but this circumstance becomes significant only after the formation of the bubble. The molecular dynamics description of water [23, 24] gives the mechanical characteristics (density and speed of sound) close to the real values and the melting temperature and T_c slightly below than the values in natural water. The molecular dynamics thermal conductivity is the same in order of magnitude as in natural water in wide density and temperature ranges.

Because of a finite thermal conductivity, the molecular dynamics simulation allows the heating of the liquid from the hot target. The typical situation is demonstrated in Figs. 5–7. The ultrashort heating generates two shock waves (cf. Figs. 3, 4). We consider phenomena in near-interface region 2. At the time shown in Figs. 5–7, the pressure in this region is 4 kbar, which is an order of magnitude higher than the critical pressure p_c. A small increase in the pressure on the left edge of the 2–N plate is due to an acoustic wave traveling inside the plate [25–28]. Spatial beatings of the profile in the crystal phase (to the right of the melting region 3–4 in Figs. 5 and 6) are due to the smallness of the grid step, which is comparable with the period of the crystal lattice.

Because of the heating of water in view of heat conduction, the breakdown of the junction as in the

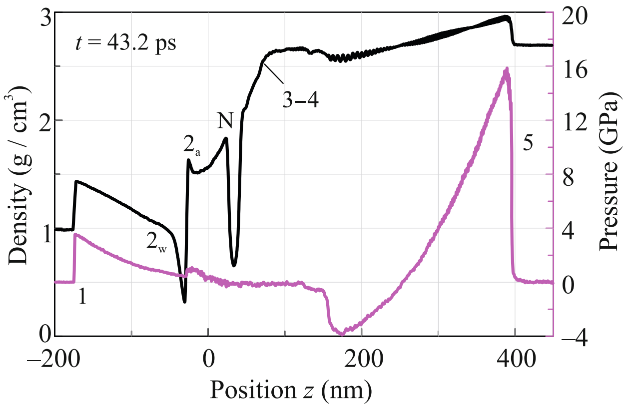

Fig. 5. (Color online) Density and pressure profiles in the molecular dynamics simulation. The meaning of marks 1–5 is the same as in Fig. 3; N is the nucleation region; and 2_a–N is the separating plate, which would be separated at $F_{abs} > F_a$. In this calculation, $F_{nucl} < F_{abs} < F_a$; i.e., nucleation occurs, but the plate is not separated.

hydrocode is absent (cf. Figs. 3 and 4). Correspondingly, the pressure in region 2 does not vanish, but the density in it decreases significantly (see Fig. 5–7) for two reasons. The first reason is the expansion of gap 2 because of mechanical extension caused by the inertia of water and by the deceleration of the boundary of the target (as in the hydrocode). The second reason is the characteristic pressure of hot water in region 2. It is seen that the first reason is more important because the gradient of the pressure in Fig. 5 is opposite to the expansion.

The size of the microbubble can be estimated from the mass balance (this is the main aim of this section). The mass balance has the form $\rho_{hw}\pi R_L^2 z_T = \rho_g(4/3)\pi R^3$. The left-hand side is the mass of the disk with the radius $R_L = 3$ μm (radius of the Gaussian beam) and thickness z_T. This thickness is indicated in Fig. 7 by red arrows at a temperature of 4 kK. The disk is filled with hot water with the density $\rho_{hw} \approx 0.3$ g/cm^3 (see Fig. 7). The right-hand side of the mass balance is the mass of the bubble with the radius R, where the gas has the density ρ_g. Therefore,

$$R/R_L = 0.9(A/\Gamma)^{1/3}, \quad A = \rho_{hw}/\rho_g, \quad \Gamma = R_L/z_T.$$

The ratio of the radii R/R_L is determined by the ratio of two large parameters (both about 10^3): the ratio A of the density about the density of the condensed phase to the density of the gas at a pressure of about 1 atm) and the geometric factor Γ. The pressure in the bubble with a radius of 500 nm in glycerol is 3.4 atm (1 atm is the ambient pressure and 2.4 atm is the pressure $2\sigma/R$).

At the first oscillation of millimeter-size bubbles [29, 30], they primarily contain evaporated liquid. The volume is calculated using the adiabats of the liquid, which are continued to a pressure of 1 atm (see Fig. 11 in [13]). In our situation with microbubbles with the radius $R \sim 1$ μm, the mean free path of a vapor molecule is about R, which corresponds to the Knudsen regime: the molecule passes through the bubble in a time of about 10 ns. The vapor bubble obviously cannot exist for 200 μs because both the liquid and the target are cooled to room temperature in this time and vapor is condensed. Thus, the bubble should be filled with gaseous products of the decomposition of glycerol.

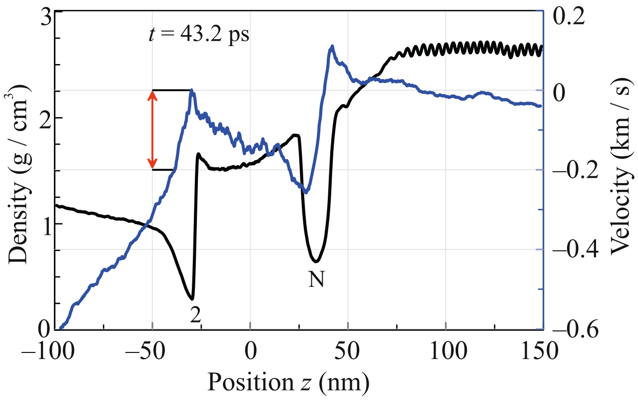

Fig. 6. (Color online) Pressure of heated water in region 2 promotes the expansion of this region in the molecular dynamics simulation. The double red arrow gives an expansion rate of 200 m/s.

The decomposition of glycerol apparently occurs in a nanolayer near the hot wall (see red arrows in Fig. 7). The authors of [31] studied the formation of gas (not vapor) bubbles at ablation in the liquid. It is currently unclear what mass fraction of this hot layer will remain in the gas state for times of hundreds of microseconds in our experiments. A decrease in this fraction below unity in the above mass balance relation (left-hand side) reduces the radius of the bubble R.

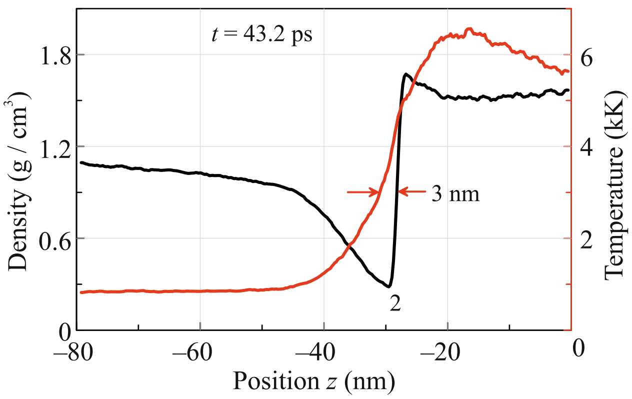

Fig. 7. (Color online) Molecular dynamics distribution of the temperature in hot near-interface layer 2 (see also Fig. 6). The width of the separation region indicated for $T > 3$ kK is 3 nm.

4. ELECTRODYNAMIC SIMULATION

The simulation was performed by the finite element method with Comsol Multiphysics software. The problem of the incidence of the Gaussian beam with the radius $R_L = 3$ μm on silicon was solved in axisymmetric geometry for right and left circularly polarized Gaussian beams. Then, using two solutions for circularly polarized Gaussian beams, we constructed a solution for a linearly polarized Gaussian beam (implemented in the experiment).

The numerical simulation was performed for two cases. The first case corresponds to the irradiation of the surface of silicon by the first femtosecond laser pulse. In this case, the light pulse is incident on the surface of silicon from the homogeneous glycerol layer. The second case corresponds to the irradiation of the surface of silicon by the second femtosecond laser pulse. In this case, the gas bubble (with the center on the axis of incidence of the pulse) in the form of a sphere or truncated sphere with the radius R and distance d from the surface of silicon to the center of the sphere is located above the surface of silicon (see Fig. 1). The refractive indices of silicon, glycerol, and gas at $\lambda = 1028$ nm are $3.566 + 2.6 \times 10^{-4} i$, 1.46, and 1, respectively.

The spatial distribution of the power absorbed in silicon was calculated in the problem for the first femtosecond laser pulse. The maximum (on the beam axis) intensity I_G of the electric field in silicon at a depth of 20 nm and at a given energy of the pulse was found. Further, this parameter was used to normalize the spatial redistribution of the intensity of the second pulse in silicon.

The simulation of the incidence of the second pulse on the surface of silicon in the presence of the gas bubble in glycerol gave the three-dimensional intensity distribution $I(r, z)$ for the electric field of the second pulse in silicon, where r is the radius measured from the axis and z is the distance to the surface of silicon along the normal to it. Thus, neglecting nonlinear optical effects, the normalized distribution $I(r, z)/I_G$ is independent of the energy of the pulse (the energies of the first and second pulses are the same). An example of the calculation is demonstrated by the red line in Figs. 1 and 2.

5. MOLECULAR DYNAMICS

The direct atomistic simulation of glycerol and silicon is strongly complicated because the interatomic interaction in these materials, as well as the interaction between a Si atom and a glycerol molecule, is complex. For this reason, the molecular dynamics simulation was performed for a pair of materials with close mechanical parameters: the density and speed of sound. Glycerol was described by the atomic model of water (molecule as a point particle) with the potential from [24], whereas silicon was simulated by the model of aluminum with the EAM potential [32]. The interatomic interaction between the water "atom" and silicon atom was described by the Lennard-Jones potential with the minimum located at the position equal to the sum of van der Waals radii of silicon (0.21 nm) and oxygen (0.152 nm) atoms and with the small depth $\varepsilon/k_B = 113$ K, as between oxygen molecules.

In the vertical (z axis) direction, the 200-nm-thick water layer covered the 200-nm-thick aluminum layer. The vertical dimension of the computation region was $L_z = 500$ nm; the upper boundary of water and the lower boundary of silicon were free with an insignificant density of water vapor above them. The horizontal dimension of the computation region was $L_x =$ 400 nm and was completely filled with the materials. Since the problem is planar, the y dimension of the region was small, $L_y = 10$ nm. Periodic boundary conditions were imposed in all three directions. The system contained approximately 48×10^6 aluminum atoms and 26×10^6 water "atoms."

Before the laser heating of aluminum, the Langevin thermostat transferred the system to mechanical and thermodynamic equilibrium at $p \approx 0$ and $T \approx 300$ K. Then, this thermostat rapidly heated the central spot on the surface of aluminum with the strip width $l_x = 160$ nm, which is about a factor of $M = 6.4$ smaller than that in the experiment shown in Fig. 2. To establish similarity between the simulation and experiment, the scaling factor M is used to determine the heating depth in the molecular dynamics simulation and to compare the calculated and experimental profiles of the aluminum/silicon surface (see Fig. 2).

The distributions of the target temperature in depth and width were chosen Gaussian and nearly Gaussian $T(x) = T_0 \cos^2(\pi x/l_x) + 300$ K, respectively. As a result, the temperature field has the form $T(x, z) = T_0 \cos^2(\pi x/l_x) \exp[-(z/h)^2] + 300$ K, where $h = 20$ nm is the heating depth and $|x| < l_x/2$. Aluminum atoms were heated for 1 ps, which is typical of the time of energy transfer from the electron to ion subsystem in aluminum. To exclude the thermostat-induced deceleration of the material in the xz plane, heating was performed only in the y velocity component. The transfer of the thermal energy to other translational degrees of freedom was due to interatomic collisions.

6. CONCLUSIONS

The features of the effect of two femtosecond laser pulses separated by a submillisecond time delay on the surface of silicon immersed in a liquid have been studied experimentally and theoretically. The specificity of such effect is that the first pulse results in the formation of a gas microbubble and the second pulse is scattered on it with the formation of a ring diffraction pattern, leading to an extraordinarily deep modulation of the surface relief.

The height of structures on silicon that are formed by this method is hundreds of nanometers at low and moderate energies of the action, which are not accompanied by a significant loss of the mass of the target. In the absence of the bubble, reliefs are much less pronounced: their height is one or two orders of magnitude lower. For applications, we note that a technically more complex alternative for the production of submicron structures is the use of ultraviolet radiation in the diffraction limit.

Using the developed theoretical and numerical model, we have obtained and explained quantitative data on the features of the formation and sizes of the gas bubble, the "weak heat conduction" mechanism, the diffraction of radiation, and the formation of the nanorelief. To solve the problem, we have developed a hybrid computational approach based on the physical specificity of the laser action in the liquid. The approach involves mutually supplementing numerical codes: hydrodynamics with real equations of state and inclusion of phase transitions, electrodynamics, and molecular dynamics of the model system.

FUNDING

V.A. Zhakhovsky, S.A. Romashevskiy, S.I. Ashitkov, and N.A. Inogamov, who performed the experiment, molecular dynamics simulation, and development of the physical model, acknowledge the support of the Russian Science Foundation (project no. 19-19-00697). V.A. Khokhlov, who performed the hydrodynamic calculation, acknowledges the support of the Ministry of Science and Higher Education of the Russian Foundation (agreement no. 075-15-2020-785 with the Joint Institute for High Temperatures, Russian Academy of Sciences).

REFERENCES

1. E. Stratakis, M. Barberoglou, C. Fotakis, G. Viau, C. Garcia, and G. A. Shafeev, Opt. Express **17**, 12650 (2009).
2. D. Zhang, B. Gokce, and S. Barcikowski, Chem. Rev. **117**, 3990 (2017).
3. A. V. Kabashin, A. Singh, M. T. Swihart, I. N. Zavestovskaya, and P. N. Prasad, ACS Nano **13**, 9841 (2019).
4. S. I. Kudryashov, A. A. Samokhvalov, A. A. Nastulyavichus, I. N. Saraeva, V. Y. Mikhailovskii, A. A. Ionin, and V. P. Veiko, Materials **12**, 562 (2019).
5. C. Unger, J. Koch, L. Overmeyer, and B. N. Chichkov, Opt. Express **20**, 24864 (2012).
6. Y. Nakata, N. Miyanaga, K. Momoo, and T. Hiromoto, Appl. Surf. Sci. **274**, 27 (2013).
7. D. S. Ivanov, A. I. Kuznetsov, V. P. Lipp, B. Rethfeld, B. N. Chichkov, M. E. Garcia, and W. Schulz, Appl. Phys. A **111**, 675 (2013).
8. N. A. Inogamov, V. V. Zhakhovskii, and V. A. Khokhlov, J. Exp. Theor. Phys. **120**, 15 (2015).
9. S. V. Starikov and V. V. Pisarev, J. Appl. Phys. **117**, 135901 (2015).
10. A. A. Kuchmizhak, A. A. Ionin, S. I. Kudryashov, S. V. Makarov, A. A. Rudenko, Yu. N. Kulchin, O. B. Vitrik, and T. V. Efimov, Opt. Lett. **40**, 1687 (2015).
11. A.Kuchmizhak, O.Vitrik, Yu. Kulchin, D. Storozhenko, A. Mayor, A. Mirochnik, S. Makarov, V. Milichko, S. Kudryashov, V. Zhakhovsky, and N. Inogamov, Nanoscale **8**, 12352 (2016).
12. Yu. V. Petrov, V. A. Khokhlov, V. V. Zhakhovsky, and N. A. Inogamov, Appl. Surf. Sci. **492**, 285 (2019).
13. N. A. Inogamov, V. A. Khokhlov, Yu. V. Petrov, and V. V. Zhakhovsky, Opt. Quantum Electron. **52**, 63 (2020).
14. S. A. Romashevskiy, S. I. Ashitkov, and M. B. Agranat, Opt. Lett. **45**, 1005 (2020).
15. S. A. Romashevskiy, S. I. Ashitkov, and M. B. Agranat, Appl. Phys. Lett. **109**, 261601 (2016).
16. J. M. Liu, Opt. Lett. **7**, 196 (1982).
17. A. V. Bushman, G. I. Kanel', A. L. Ni, and V. E. Fortov, *Intense Dynamic Loading of Condensed Matter* (Taylor and Francis, Washington, DC, 1993).
18. K. V. Khishchenko, High Temp. **35**, 991 (1997).
19. I. V. Lomonosov, Laser Part. Beams **25**, 567 (2007).
20. I. V. Lomonosov, V. E. Fortov, and Ya. B. Zel'dovich, Phys. Usp. **57**, 219 (2014).
21. K. V. Khishchenko, Math. Montis. **40**, 140 (2017).
22. R. I. Nigmatulin and R. Kh. Bolotnova, High Temp. **49**, 303 (2011).
23. N. A. Inogamov, V. V. Zhakhovskii, and V. A. Khokhlov, J. Exp. Theor. Phys. **127**, 79 (2018).
24. V. V. Zhakhovsky, Tabulated EAM Potential for Water. www.researchgate.net/project/Development-of-interatomic-EAM-potentials.
25. T. Antoun, L. Seaman, D. R. Curran, G. I. Kanel, S. V. Razorenov, and A. V. Utkin, *Spall Fracture: ShockWave and High Pressure Phenomena* (Springer, New York, Berlin, Heidelberg, 2003).
26. G. I. Kanel, S. V. Razorenov, and V. E. Fortov, *Shock-Wave Phenomena and the Properties of Condensed Matter* (Springer, New York, Berlin, Heidelberg, 2004).
27. G. I. Kanel', V. E. Fortov, and S. V. Razorenov, Phys. Usp. **50**, 771 (2007).
28. B. J. Demaske, V. V. Zhakhovsky, N. A. Inogamov, and I. I. Oleynik, Phys. Rev. B **82**, 064113 (2010).
29. J. Lam, J. Lombard, Ch. Dujardin, G. Ledoux, S. Merabia, and D. Amans, Appl. Phys. Lett. **108**, 074104 (2016).
30. K. Sasaki and N. Takada, Pure Appl. Chem. **82**, 1317 (2010).
31. M.-R. Kalus, N. Bäsch, R. Streubel, E. Gökce, S. Barcikowski, and B. Gökce, Phys. Chem. Chem. Phys. **19**, 7112 (2017).
32. V. V. Zhakhovskii, N. A. Inogamov, Yu. V. Petrov, S. I. Ashitkov, and K. Nishihara, Appl. Surf. Sci. **255**, 9592 (2009).

Translated by R. Tyapaev